This is a preprint, the final version is subject to change, of the American Mineralogist (MSA)
Cite as Authors (Year) Title. American Mineralogist, in press.
DOI: https://doi.org/10.2138/am-2019-7074

Revision 7074-1

Identification of interstratified mica or pyrophyllite monolayers within chlorite using advanced scanning/transmission electron microscopy

Guanyu Wang[1,2], Hejing Wang[1*], Jianguo Wen[2*]

[1]School of Earth and Space Sciences, Peking University, Beijing 100871, China

[2]Center for Nanoscale Materials, Argonne National Laboratory, Lemont, IL 60439

Hejing Wang: hjwang@pku.edu.cn

Jianguo Wen: jwen@anl.gov

ABSTRACT

Interstratified clay mineral reflects weathering degree and records climatic conditions and the pedogenic processes in the soil. It is hard to distinguish a few layers of interstratified clay mineral from the chlorite matrix, due to their similar two-dimensional TOT structure and electron-beam sensitive nature during transmission electron microscopy (TEM) imaging. Here, we used multiple advanced TEM techniques including low-dose high resolution TEM (HRTEM), high-angle annular dark field scanning transmission electron microscopy (HAADF-STEM) imaging combined with energy dispersive spectroscopic (EDS) mapping to study interstratified layers in a chlorite sample from Changping, Beijing, China. We demonstrated an interstratified mica or pyrophyllite monolayer could

be well distinguished from the chlorite matrix by projected atomic structures, lattice spacings and chemical composition with advanced TEM techniques. Further investigation showed two different transformation mechanisms from mica or pyrophyllite to chlorite: either a 4 Å increase or decrease in lattice spacing. This characterization method can be extended to other electron-beam sensitive minerals.

Keywords: Chlorite; Interstratified layer; HRTEM; STEM

This is a preprint, the final version is subject to change, of the American Mineralogist (MSA)
Cite as Authors (Year) Title. American Mineralogist, in press.
DOI: https://doi.org/10.2138/am-2019-7074

INTRODUCTION

Clay minerals are phyllosilicate with the basic structure of an octahedral sheet (O sheet, marked by red dashed box in Fig. 1) sandwiched by two tetrahedral sheets (T sheet). The main constituent of the two T sheets is Si^{4+} which sometimes substituted by Al^{3+}. Mg, Fe, Al are common O sheet cations with important substitution of Cr, Ni, Mn, V, Cu, Zn etc. (Bailey, 1988). According to the difference in the interlayer (I sheet, marked by red solid box in the right in Fig. 1), some clays have no interlayer cation such as talc and pyrophyllite. Some have interlayer cations K, Na etc. countering the imbalance electricity caused by the Al^{3+} substitution to Si^{4+} in the tetrahedral sheets, such as mica. Other clay mineral such as chlorite has brucite-like sheets (B sheet, marked by red solid box in the left in Fig. 1) in the interlayer. Due to the above differences, the lattice fringes of pyrophyllite, mica and chlorite are 9.5, 10 and 14 Å respectively.

Mixed layer clays, as intermediate products of clay mineral transition and weathering, ubiquitously present in nature. Since Hendricks and Teller (1942) first mentioned partially ordered stacking layers in micas and other similar minerals, interstratified clays such as illite-montmorillonite, chlorite-vermiculite, illite-chlorite-montmorillonite etc. were abundantly reported in sedimentary rocks (Weaver, 1956; Reynolds and Hower, 1970; Bettisonvarga, 1997; Banfield and Murakami, 1998). Changes in weathering degree and climatic conditions generate the pre-existing clay phases to transform into

other species through a sequence of intermediate interstratified phases. Consequently, mixed layer clay minerals indicate the pedogenic processes that have occurred in the soil and provide a progressive structural and compositional transformation sequence of the solid-state reaction (Hong et al., 2012). Both regular and random 1:1 interstratifications of 24 Å clays (referring to a combination of contiguous 14 Å lattice and 10 Å lattice) were reported in weathering reactions or transition process (Środoń, 1999). Such mixed layer clays includes chlorite/mica (Lee and Peacor, 1985; Cruz, 2001), chlorite/talc (Schreyer et al., 1982; Ahn et al., 1988), chlorite/pyrophyllite (Kong et al., 1990; Kong et al., 1992; Kong et al., 2000) and chlorite/biotite (Veblen, 1983; Xu et al., 1996).

Due to their high similarity in structure and composition to the end-member clays, it is hard to identify the mixed layer minerals. Traditionally, they were revealed by petrographic methods, chemical methods, X-ray powder diffraction (XRD) and TEM (Środoń, 1999). For nearly a century, XRD remained as one of the most widely used tools of mixed layer clay identification, quantification, nomenclature and ordering research (Moore and Reynolds, 1989). Typically, different mixed layer clay minerals perform differently in the low-angle region of the XRD pattern for ethylene glycol-treated samples (Środoń, 1981). Over the past fifty years, conventional TEM together with HRTEM and analytical electron microscopy (AEM) were widely applied to identify the lattice spacing and bulk crystal composition (Środoń et al., 1990). Most researchers used lattice fringes

combined with XRD patterns to identify bulk mixed layer clay minerals (Shau et al., 1990; Środoń et al., 1990; Arroyo et al., 2018; Hoang-Minh et al., 2019). Scanning transmission-electron microscopy (STEM) also applied to the investigation of phyllosilicates (Shen et al., 1988; Kameda et al., 2009; Inoué and Kogure, 2016). HAADF-STEM image is a Z-contrast image, whose contrast is roughly proportional to the square of average atomic number (Z), offering detailed cations distribution information (Inoué and Kogure, 2016).

However, of all above methods, specimen for XRD is easy to prepare and easy to obtain, but it fails to provide individual crystal information as the tool averages millions of crystals. In order to characterize the specific nature of an individual interstratified clay layer or a packet of interstratified layers, it is necessary to directly image layers using TEM techniques (Lee et al., 1984). Viewing the interstratified layers via TEM/STEM requires edge on direction, which is hard to obtain due to the preferred orientation of these scaly clay minerals. The existence of hydroxyl in their crystal structures also adds difficulty in obtaining high quality images for even necessary tilting is improbable because of the severe e-beam damage. Therefore, for ordered interstratified clays with consistent crystal structure and chemical composition, bulk crystal information and limited TEM images can provide some information, whereas, for the few layers of non-regular repeated intermediate products, which are more common in nature, it is hard

to differentiate them from the matrix using these methods.

In the present work, we utilized multiple advanced TEM techniques including HRTEM, HAADF imaging combined with EDS mapping to identify small amount of irregularly repeated mixed layer clay minerals in a chlorite sample from Changping, Beijing and then investigated the intergrowth mechanism. We verified the new approach could help to identify the interstratified mica or pyrophyllite monolayer from chlorite via lattice spacing, HRTEM images, HAADF images and EDS mapping. We expect this characterization method can be well extended to other e-beam sensitive materials.

MATERIALS AND METHODS

The sample was collected from Changping, Beijing, China. The sample was prepared by cutting a chlorite-rich section from the rock chip. Those with little quartz were crushed with a hammer and further ground into powder with a hammer mill. Stoke's law was used to concentrate the < 2 μm fractions. Random and oriented powder samples were prepared for XRD. Rock chips were directly used for scanning electron microscopy (SEM) and Electron Probe Microanalyzer (EPMA). For TEM samples, the rock chip was thinned by argon milling using a Gatan 695 PIPS II under the conditions of 4.5 keV and 6° incident angle until perforation, followed by 0.2 keV milling for 0.5 h for final polishing.

This is a preprint, the final version is subject to change, of the American Mineralogist (MSA)
Cite as Authors (Year) Title. American Mineralogist, in press.
DOI: https://doi.org/10.2138/am-2019-7074

Powder XRD patterns were collected using an X'Pert Pro MPD diffractometer with an X'Celerator detector. The measuring conditions of XRD were Cu Kα radiation (λ = 1.54056 Å), 40 kV and 40 mA, 5–75° (2θ) scanning range, 0.017° (2θ) step size. Field emission scanning electron microscope (FESEM) measurement was performed with a QUANTA-650FEG microscope operating at 10 kV. Chemical composition was obtained by a JXA-8100 EPMA at 15 kV and 1×10^{-8} A, beam spot diameter 1-2 μm. TEM and HRTEM images were taken using a transmission electron microscope called Argonne Chromatic Aberration-corrected TEM (ACAT) operated at 80 kV with a low-dose rate of ~20 e^-/ $Å^2$s. Typically, 50~100 images were taken under low-dose imaging conditions at high magnification, then, all images without noticeable beam-damage effects were aligned to remove image drift and summed together for a final HRTEM image. ACAT is equipped with an image corrector to correct both spherical and chromatic aberrations to ensure an information limit better than 0.1 nm at 80 kV. HAADF-STEM images and EDS mapping were taken on a FEI Talos TEM with 200 kV accelerate voltage. The recorded TEM images were processed using a Wiener-filter implemented in a Gatan Digital Micrograph to remove noise contrast. HRTEM image simulation was carried out using a MacTempas software.

XRD analysis shows that the sample is dominated by chlorite and small amounts of quartz. SEM images show that the chlorite crystals are generally scaly in shape with

about 5 μm population size in diameter. The EPMA analysis reveals that the average structural formula is:

$Na_{0.07}K_{0.40}(Fe^{2+}_{2.52}Mg_{0.80}Ca_{0.07}Al_{1.80}\square_{0.34})_6(Si_{3.32}Ti_{0.01}Al_{0.67})_4O_{10}(OH)_8$,

assuming that the total iron is ferrous and the number of oxygen atoms is 14, and where □ denotes the vacancy.

RESULTS

Distinguishing phases using lattice spacing and SAED

XRD and EPMA compositional analyses only show the existence of chlorite, while from the low magnification TEM image (Fig. 2a), the existence of distinct lattice spacings indicated the presence of extra phases with different lattice spacing from that of chlorite. These phases are in an almost consistent orientation between each crystal without clear crystal boundaries. However, small-scale variations in crystal orientation also exist, which was revealed by the relatively different contrasts in sub-parallel crystal packets. Amorphous zones damaged by the electron beam showed no contrast and lattice (traced by the dashed lines in Fig. 2a). Several lattice defect zones (traced by the solid lines in Fig. 2a) were also captured where cracks well extended along the lattice fringes without any structural discontinuity.

A higher magnification lattice image (Fig. 2b) shows dominant 14 Å lattice spacing and a

few 10 Å lattice spacing in between. Combined with XRD and EPMA compositional analyses above, the 14 Å lattice can be assigned to chlorite. However, it is hard to determine which phase corresponds to the 10 Å lattice, since three possible clay minerals like mica, talc and pyrophyllite have a 10 Å lattice. Successive 14 Å lattices are commonly observed, indicating the chlorite is dominant. The observation of successive 10 Å lattices are absent and those 10 Å phases appear only as a monolayer adjacent to the 14 Å chlorite. The interface between 14 Å and 10 Å phases are atomically sharp, showing a consistent orientation. Previous investigations showed 24 Å chlorite/mica, chlorite/talc and chlorite/pyrophyllite interstratification. As exhibited in Fig. 2b, the irregular repeated 24 Å intermediate products (intergrowth of a 10 Å unit and a 14 Å chlorite layer) occur commonly in the sample. However, as there is no successive 10 Å lattice area, it is extremely difficult to characterize the 10 Å phase using compositional analysis and impossible by selected-area electron diffraction (SAED).

SAED pattern (Fig. 3b) of distinct lattice spacings area shows more than three order reciprocal lattice rows with $k \neq 3n$, and the average distance between lattice rows is 0.216 1/Å. The irrational *00l* diffractions and streaking *h0l* diffractions formed the "defective electron diffraction patterns" reported by Li and Wang (2019), they considered these patterns are caused by many factors including defects (Kogure and Murakami, 1998) and local disorders (Spinnler et al., 1984) such as spacing variation or the fast electron

radiation damage. In our study, the contribution from the fast electron radiation damage can be ruled out since SAED used an extremely low dose rate below 0.5 $e^-/Å^2s$. Due to spacing variation caused by the random interlayering between different phases, the reciprocal-lattice rod lengthened thus inducing the streaking of *00l* diffractions and *h0l* diffractions in Fig. 3b. And the more striking streaking of *h0l* diffractions than *00l* diffractions are due in part to the defects in Fig. 3a. The small arc-like *00l* diffractions furthermore developing into two sets of *00l* diffractions are resulted from the planner defects where the *00l* plane on either side is not parallel to each other but inclined a small angle. An intensity profile in Fig. 3c along the *00l* diffractions reveals different periodic peaks of 14 and 24 Å phases. The strong 14 Å periodic peaks correspond to intense diffraction, indicating 14 Å phase dominates.

As lattice images can be conveniently obtained in thick area and does not require tilting sample to exact zone-axis, these images are commonly observed within the studied specimens and can be easily captured with less beam damage. However, this also results in missing important information to identify exact crystal structure and phases. SAED can help to determine the periodicity and the dominant phase, but it fails to provide information about how many layers of each phase there are. Therefore, additional TEM analytical characterization are still needed to complete the identification.

This is a preprint, the final version is subject to change, of the American Mineralogist (MSA)
Cite as Authors (Year) Title. American Mineralogist, in press.
DOI: https://doi.org/10.2138/am-2019-7074

Distinguishing phases using HAADF

HAADF image shows different phases with both lattice spacing and different Z-contrast. The brighter fringes represent higher Z number while the darker fringes represent lower Z (Williams and Carter, 1996; Williams et al., 1998), when the HAADF collection cut-off angle is larger than 75 mrad. Significant difference in Z-contrast exists in Fig. 4a. The left part of Fig. 4a shows consistent lattice spacing with bright contrast, while the middle and right part exhibit different lattice spacings in alternatively dim and bright contrast. In Fig. 4a, two types of lines are identified: the first type (marked as arrows in Fig. 4b) are bright lines (formed by continuous bright spots) with nearly identical contrast, and the second type (marked as arrows in Fig. 4c) are relatively dim lines. Between the two bright (or dim) lines, there is a bright (or dark) band (marked as asterisk in Fig.4b and Fig.4c, respectively). Considering crystal structure information, the bright lines and bands can be assigned to the 14 Å chlorite. The bright lines are the octahedral sheets (both O sheets and B sheets) of chlorite while the bright bands represent the tetrahedral sheets (T) of chlorite. In the magnified image Fig.4b, the integrated contrast of the B sheets is a little brighter than that of the O sheets, which means B sheets have more higher Z number atoms (Fe in this sample) than O sheets. The contrast ratios of the dim lines and bands (about 10 Å as a whole) imply the average Z numbers of occupied cations in the 10 Å layers has lighter cations than that in the 14 Å layers. Combined the HAADF images with chemical composition of different clays minerals, the 14 Å chlorite in this sample has Fe

in the octahedral sites, while common 10 Å clay minerals such as micas, talc, pyrophyllite usually has no or less atoms with Z number as high as Fe. However, it is still unclear what the 10 Å phase is.

The chlorite layers, consisting of more than 20 consecutive 14 Å chlorite layers (right part of Fig. 4a), are well-developed without much edge dislocations or other defects. The 10 Å layers are subparallel or nearly subparallel to the 14 Å chlorite layers, implying they are parts of the same phyllosilicate crystal. Fig. 4d shows a change from brighter line to darker line, demonstrating a distinct transformation from 28 (14 + 14) Å to 24 (10 + 14) Å with a B sheet termination. Detailed transformation mechanism will be discussed in the following section.

Distinguishing phases using HRTEM

According to the unique lattice spacing, distance and angle between adjacent spots and columns, HRTEM image confirms the predominant 14.3 Å phase is chlorite. Chlorite can be classified into four subgroups according to the octahedral structure of both TOT layers and B sheets. The smallest TOT structural unit (half) contains three octahedral sites. When they are all occupied by divalent cations, it is known as trioctahedral, while if only two are occupied by trivalent cations, it is dioctahedral (Wang et al., 2017). Trioctahedral chlorite, the most common form, refers to both O and B sheets are trioctahedral. When cations in O and B sheets are all trivalent, it belongs to dioctahedral chlorite. If O sheet is

dioctahedral but B sheet is trioctahedral or otherwise, it belongs to di-, trioctahedral or tri-, dioctahedral, respectively (Bailey, 1988). Whether a mineral is dioctahedral or trioctahedral can be determined by HRTEM. Under current resolution condition, dioctahedral sheet can be identified as dots for it has fewer cations, while trioctahedral sheet appears as a line. As it can be seen from Fig. 5a, tetrahedral sheets appear as bright dots while the octahedral sheets (thinner bright stripes) and brucite-like sheets (thicker bright stripes) appear as both lines and dots, implying the octahedral sheets are dioctahedral but in some areas trioctahedral. Fig. 5b reveals single ~10 and ~9.5 Å layers interleaved within the dominant 14.3 Å chlorite. The ~9.5 Å phase without interlayer cations is probably pyrophyllite or talc. Pyrophyllite is dioctahedral with Al^{3+} occupied the octahedral sites, while talc is trioctahedral with Mg^{2+} occupied the octahedral sites. As dots can be seen in the octahedral sheet of ~9.5 Å phase and the crystal structure fits well with that of pyrophyllite (Cruz et al., 2004; Cruz and De Galdeano, 2005), it is probably pyrophyllite. The ~10 Å phase with interlayer cations may be mica. Simulated image using major simulation parameters (thickness 6 nm, Δf = -20 nm, C_s = 10 μm) confirms the above results. However, as these layers are rare and more likely to appear as a single layer, it is hard to identify their composition by EDS, so HAADF with EDS mapping was used for further verification.

Distinguishing phases using HAADF+EDS

As discussed above, the bright lines with bright bands in HAADF are 14 Å chlorite while the dimmer lines with dim bands correspond to ~10 Å phases. EDS Mapping results and element profile are shown in Fig. 6a and 6b, respectively. In Fig. 6a, the 14 Å area is marked with area 1 and the ~10 Å areas are marked as area 2, 3. EDS mapping shows that the ~10 Å areas 2 and 3 have lower Fe, and area 3 has higher K content than the 14 Å area 1. Semi-quantitative analysis in Table 1 further supports the area 2 has a decrease in Fe content and correspondingly a slight enrichment in Al and Si. Combined with HRTEM results above (the ~9.5 Å phase is locally dioctahedral without interlayer cations), the phase can be identified as pyrophyllite. In the area 3, mapping images and element profile show characteristic K with lower Fe, Al signals and a slight increase of Si content than chlorite. Qualitative analysis also indicates the existence of K. Combined with HRTEM results above (the ~ 10 Å phase has interlayer cations), the phase is identified as mica.

DISCUSSION

Identification of interstratified mica or pyrophyllite monolayer from chlorite

Using multiple TEM techniques combined HRTEM, STEM with EDS mapping, three mineral phases can be well identified as above demonstrated. HAADF is lattice spacing and contrast sensitive, TEM (combined with HRTEM) is sensitive to lattice spacing and atomic column arrangement, and EDS is helpful in identifying characteristic elements.

Table 2 shows a brief summary of the difference between mica, pyrophyllite and chlorite in lattice spacings and appearances under different imaging conditions. Using these three mineral phases as an example, Fig. 7 illustrates how the interstratified mica or pyrophyllite monolayer was identified from chlorite. Firstly, TEM and HAADF shows the lattice spacing, then SAED determines crystal orientation. Afterwards, low-dose HRTEM helps to obtain atomic position and arrangement. In this case, the two ~ 10 Å phases arrange distinctively regarding the interlayer cation. Apart from structural differences revealed by lattice spacing and atomic arrangement, compositional differences was revealed by EDS to identify the characteristic elements in these phases. This method can be well applied to the identification of other layer structure materials.

Intergrowth mineral reaction

Although much has been learnt about the transition from mica to chlorite, the detailed structural change during the transformation has not been reported by HRTEM. From Fig. 8a, a clear transformation from 24 to 28 Å indicates an increase in volume. It can be seen from the magnified image that such a transition involves a termination of the brucite-like sheet between two adjacent chlorite TOT layers; sometimes such a termination is also accompanied with a lattice distortion. Two mechanisms involving volume increase during the transformation from mica/semctite to chlorite have been raised (Veblen, 1983; Veblen and Ferry, 1983; Xu et al., 1996; Bettisonvarga, 1997). The first mechanism proposed a 14 Å spacing increase, which involves the dissolution of one T-O-T layer and then

282 followed by the T-O-T B T-O-T unit reprecipitation. In this case, the spacing increase
283 should be 14 Å rather than 4 Å. The second mechanism concerns the growth of a
284 brucite-like sheet into the interlayer region between two TOT mica layers and a 4 Å
285 spacing increase, which fits well with Fig. 8a.
286
287 Another transformation involves volume decrease with the lattice spacing change from 32
288 to 28 Å. One mechanism was proposed to concern the volume decrease before (Veblen
289 and Ferry, 1983). It considers the formation of a brucite-like sheet by removal of the two
290 tetrahedral sheets of one TOT mica layer, where the spacing decrease should be ~8 Å.
291 Dash line in the middle of Fig. 8b shows two lines terminate into one brucite-like sheet
292 involving 4 Å spacing decrease. This intermediate product demonstrates the transition
293 from the TOT mica layer to a brucite-like sheet is a gradually reaction, and the two T
294 sheets are dissolved step by step.

295 **IMPLICATION**

296 Irregular mixed layer clay minerals are common in nature. Since different interstratified
297 mineral phases appear only as few layers, they are difficult to identify by conventional
298 methods such as XRD or TEM. We developed a new method combining multiple
299 advanced TEM techniques (HRTEM, STEM with EDS) to identify mixed layers in a
300 chlorite sample. Via lattice spacing, HRTEM images, HAADF images and EDS mapping,

301 we distinguished the parallel-growing monolayer mica and pyrophyllite from chlorite
302 domains. This method can be well extended to other minerals, especially these e-beam
303 sensitive minerals. The application of the above low-dose TEM techniques provides
304 detailed structural and compositional information with minor damage, which is of great
305 importance to the identification and characterization of mixed layer minerals and the
306 study of weathering process.
307

308 **ACKNOWLEDGEMENTS**

309 We thank Jock Churchman (University of Adelaide, Australia) for constructive comments
310 and suggestions that improved our manuscript. This work was supported by the National
311 Natural Sciences Foundation of China [Grant No: 41872048, 41372061, 40972038].
312 Electron microscopy was performed at the Center for Nanoscale Materials at Argonne
313 National Laboratory, a U.S. Department of Energy Office of Science Laboratory operated
314 under Contract No. DE-AC02-06CH11357 by UChicago Argonne, LLC. Guanyu Wang is
315 grateful for the financial support from China Scholarship Council (No. 201806010080)
316 and technical support from Duan Luo.

317 **REFERENCES CITED**

318 Ahn, J.H., Peacor, D.R., and Coombs, D.S. (1988) Formation mechanisms of illite,
319 chlorite and mixed-layer illite-chlorite in Triassic volcanogenic sediments from the

Southland Syncline, New Zealand. Contributions to Mineralogy and Petrology, 99, 82-89.

Arroyo, X., Rey, J.J., Fernández, A.M., Arostegi, J., and Nieto, F. (2018) Application of the alkylammonium method to determine the layer charge of the expandable component of mixed-layer Chlorite/Smectite. EGU General Assembly Conference Abstracts, 20, p. 19188.

Bailey, S.W. (1988) Chlorites; structures and crystal chemistry. Reviews in Mineralogy and Geochemistry, 19, 347-403.

Banfield, J.F., and Murakami, T. (1998) Atomic-resolution transmission electron microscope evidence for the mechanism by which chlorite weathers to 1:1 semi-regular chlorite-vermiculite. American Mineralogist, 83, 348-357.

Bettisonvarga, L. (1997) The Role of Randomly Mixed-Layered Chlorite/Smectite in the Transformation of Smectite to Chlorite. Clays & Clay Minerals, 45, 506-516.

Cruz, M.D.R. (2001) Mixed-layer mica-chlorite in very low-grade metaclastites from the Maláguide Complex (Betic Cordilleras, Spain). Clay Minerals, 36, 307-324.

Cruz, M.D.R., and De Galdeano, C.S. (2005) Compositional and structural variation of sudoite from the Betic Cordillera (Spain): A TEM/AEM study. Clays and Clay Minerals, 53, 639-652.

Cruz, M.D.R., Morata, D., Puga, E., Aguirre, L., and Vergara, M. (2004) Microstructures and interlayering in pyrophyllite from the Coastal Range of central Chile: evidence

of a disequilibrium assemblage. Clay Minerals, 39, 439-452.

Hendricks, S., and Teller, E. (1942) X-ray interference in partially ordered layer lattices. The Journal of Chemical Physics, 10, 147-167.

Hoang-Minh, T., Kasbohm, J., Nguyen-Thanh, L., Nga, P.T., Lai, L.T., Duong, N.T., Thanh, N.D., Thuyet, N.T.M., Anh, D.D., and Pusch, R. (2019) Use of TEM-EDX for structural formula identification of clay minerals: a case study of Di Linh bentonite, Vietnam. Journal of Applied Crystallography, 52, 133-147.

Hong, H., Churchman, G.J., Gu, Y., Yin, K., and Wang, C. (2012) Kaolinite–smectite mixed-layer clays in the Jiujiang red soils and their climate significance. Geoderma, 173, 75-83.

Inoué, S., and Kogure, T. (2016) High-angle annular dark field scanning transmission electron microscopic (HAADF-STEM) study of Fe-rich 7 Å–14 Å interstratified minerals from a hydrothermal deposit. Clay Minerals, 51, 603-613.

Kameda, J., Sugimori, H., and Murakami, T. (2009) Modification to the crystal structure of chlorite during early stages of its dissolution. Physics and Chemistry of Minerals, 36, 537-544.

Kogure, T., and Murakami, T. (1998) Structure and formation mechanism of low-angle grain boundaries in chlorite. American Mineralogist, 83, 358-364.

Kong, Y.H., Peng, X.W., and Tian, D.H. (1990) Lunijianlaite—a new regular interstratified mineral. Acta Mineralogica Sinica, 4, 289-298 (in Chinese with

English abstract).

Kong, Y.H., Peng, X.W., Tian, D.H., and Wang, Y.W. (1992) HRTEM observation of fine structure of lunijianlaite. Acta Mineralogica Sinica, 1, 7-13 (in Chinese with English abstract).

Kong, Y., Wu, F., Huang, H., Jiang, L., and Wang, J. (2000) Self-organized genesis of Lunijianlaite and its apparent single-crystal. Science in China Series D: Earth Sciences, 43, 638-645.

Lee, J.H., and Peacor, D. (1985) Ordered 1: 1 interstratification of illite and chlorite; a transmission and analytical electron microscopy study. Clays and Clay Minerals, 33, 463-467.

Lee, J.H., Peacor, D.R., Lewis, D.D., and Wintsch, R.P. (1984) Chlorite-illite/muscovite interlayered and interstratified crystals: a TEM/STEM study. Contributions to Mineralogy and Petrology, 88, 372-385.

Li, T., and Wang, H. (2019) Lattice Row Distance and Its Application in Row-Indexing. Crystals, 9, 62.

Moore, D.M., and Reynolds, R.C. (1989) X-ray Diffraction and the Identification and Analysis of Clay Minerals. Oxford university press Oxford.

Reynolds, R.C., and Hower, J. (1970) The nature of interlayering in mixed-layer illite-montmorillonites. Clays and Clay minerals, 18, 25-36.

Rieder, M., Cavazzini, G., D'yakonov, Y.S., Frank-Kamenetskii, V.A., Gottardi, G.,

Guggenheim, S., Koval', P.V., Mueller, G., Neiva, A.M., and Radoslovich, E.W. (1998) Nomenclature of the micas. Clays and clay minerals, 46, 586-595.

Schreyer, W., Medenbach, O., Abraham, K., Gebert, W., and Müller, W. (1982) Kulkeite, a new metamorphic phyllosilicate mineral: Ordered 1:1 chlorite/talc mixed-layer. Contributions to Mineralogy and Petrology, 80, 103-109.

Shau, Y.-H., Peacor, D.R., and Essene, E.J. (1990) Corrensite and mixed-layer chlorite/corrensite in metabasalt from northern Taiwan: TEM/AEM, EMPA, XRD, and optical studies. Contributions to Mineralogy and Petrology, 105, 123-142.

Shen, P.Y., Hwang, S.L., Chu, H.T., and Jeng, R.C. (1988) STEM study of "ferritchromit" from the Heng-Chun chromitite. American Mineralogist, 73, 383-388.

Spinnler, G.E., Self, P.G., Iijima, S., and Buseck, P.R. (1984) Stacking disorder in clinochlore chlorite. American Mineralogist, 69, 252-263.

Środoń, J. (1981) X-ray identification of randomly interstratified illite-smectite in mixtures with discrete illite. Clay Minerals, 16, 297-304.

Środoń, J. (1999) Nature of mixed-layer clays and mechanisms of their formation and alteration. Annual Review of Earth and Planetary Sciences, 27, 19-53.

Środoń, J., Andreoli, C., Elsass, F., and Robert, M. (1990) Direct high-resolution transmission electron microscopic measurement of expandability of mixed-layer illite/smectite in bentonite rock. Clays and Clay Minerals, 38, 373-379.

Veblen, D.R. (1983) Microstructures and mixed layering in intergrown wonesite, chlorite,

talc, biotite, and kaolinite. American Mineralogist, 68, 566-580.

Veblen, D.R., and Ferry, J.M. (1983) A TEM study of the biotite-chlorite reaction and comparison with petrologic observations. American Mineralogist, 68, 1160-1168.

Wang, G., Wang, H., and Zhang, N. (2017) In situ high temperature X-ray diffraction study of illite. Applied Clay Science, 146, 254-263.

Wardle, R., and Brindley, G. (1972) The crystal structures of pyrophyllite, 1Te, and of its dehydroxylate. American Mineralogist, 57, 732-750.

Weaver, C.E. (1956) The distribution and identification of mixed-layer clays in sedimentary rocks. American Mineralogist, 41, 202-231.

Williams, D.B., and Carter, C.B. (1996) The transmission electron microscope. Transmission electron microscopy, p. 3-17. Springer.

Williams, D.B., Carter, C.B., and Veyssiere, P. (1998) Transmission electron microscopy: a textbook for materials science. Springer.

Xu, H., Zhang, Y., and Veblen, D.R. (1996) Periodic and nonperiodic interstratification in the chlorite-biotite series. American Mineralogist, 81, 1396-1404.

List of figure captions

Figures:

Fig. 1 Schematic crystal structure of chlorite (left), mica (middle) and pyrophyllite (right). T-sheet refers to tetrahedral sheet; O-sheet refers to octahedral sheet marked by red dashed box; I-sheet refers to interlayer marked by red solid box in the right; B sheet

refers to brucite-like sheet marked by red solid box in the left. Pyrophyllite has no interlayer cation, and mica has K, Na etc. as interlayer cations, while chlorite has a hydroxide sheet (B-sheet) in its interlayer

Fig. 2 (a) TEM lattice images shows distinct lattice spacings and multiple phases. **(b)** Higher magnification of TEM lattice image which are from (a) shows 10 Å phase interleaved within the dominant 14 Å chlorite

Fig. 3 (a) TEM lattice images show distinct lattice spacings and more than one phases. **(b)** SAED pattern of (a) shows more than three lattice rows with $k \neq 3n$. The pattern shows irrational *00l* diffractions with streaking non-*00l* diffractions. **(c)** An intensity profile along *00l* diffractions of (b) shows the existence of periodic 14 and 24 Å phases. The 14 Å (or 24 Å) group are marked with upward (or downward) arrows on the left (or right) of the transmission diffraction spot (0 point), respectively

Fig. 4 (a) STEM lattice images taken from the same area to the TEM images. **(b)** Magnified image of the top left rectangle (marked by 1) shows the straight and continuous 14 Å chlorite fringes, the bright lines with identical contrast (marked as arrows) are assigned to the octahedral sheets (both O sheets and B sheets) of chlorite, the integrated contrast of B sheets are a little brighter than that of the O sheets. The band (marked as asterisk) separated by two bright lines are the tetrahedral sheets of chlorite. **(c)** Magnified image of the right rectangle (marked by 2) shows the dark 10 Å phase within the 14 Å chlorite grains, the relatively dark lines (marked as arrows) represent the O

sheets and the band between (marked as asterisk) represents the T sheets. **(d)** Magnified image of the middle rectangle (marked by 3) shows a change from brighter line to darker line, demonstrating a distinct transformation from 28 (14 + 14) Å to 24 (10 + 14) Å with a termination of the B sheet

Fig. 5 (a) HRTEM image of chlorite (14.3 Å) interstratified with ~9.5 and ~10 Å phases. The brucite-like interlayer is imaged as a bright stripe (dots and lines), tetrahedral sheet as bright spots and the octahedral sheet as a thinner bright stripe (dots and lines). **(b)** Magnified image of the white rectangle in (a) and a schematic of HRTEM image. The ~9.5 Å clay phase has the TOT structure without interlayer ion. The ~10 Å clay phase has K^+ as interlayer cation. The 14.3 Å chlorite has a brucite-like sheet in the interlayer. T refers to tetrahedral sheet, marked as yellow sheets. O refers to octahedral sheet, marked as light blue sheets. B refers brucite-like sheet, marked as dark blue sheets. **(c)** Simulated image for the [100] zone of chlorite, mica and pyrophyllite with the defocus value of 200 Å and the thickness value of 60 Å

Fig. 6 (a) Mapping results show different Mg, Al, Si, K, Fe contents of 14 Å area (marked as 1) and two ~10 Å areas (marked as 2,3) within one scanning. **(b)** The element profile along the marked yellow line and the three areas 1, 2, 3 are corresponding to (a)

Fig. 7 A flow diagram shows how the interstratified mica or pyrophyllite monolayer is identified from chlorite

Fig. 8 Intergrowth mineral reaction mechanisms. **(a)** Transformation from 24 to 28 Å

460 indicating an increase in volume. Dash line in the middle shows the termination of
461 brucite-like sheet between the two adjacent chlorite TOT layers, the broken line shows
462 brucite-like sheet distortion. **(b)** Transformation from 32 to 28 Å indicating a decrease in
463 volume. Dash line in the middle shows two lines terminate into one brucite-like sheet
464 involving 4 Å spacing decrease

465 **Tables**

466 Table 1

467 STEM/EDS results (at %[a]) of the three marked area in Fig. 6.

Area	1	2	3
K			0.5 ± 0.3
Mg	3.0 ± 0.8	2.9 ± 1.0	3.7 ± 0.9
Fe	11.2 ± 1.5	8.4 ± 1.5	8.4 ± 1.2
Al	6.7 ± 1.2	8.4 ± 1.7	6.1 ± 1.1
Si	11.3 ± 1.3	13.2 ± 1.9	15.2 ± 1.5
O	67.8 ± 7.7	67.1 ± 8.5	66.1 ± 7.4
total	100.0 ± 12.6	100.0 ± 15.5	100.0 ± 12.3

468 [a]: standard deviation values are in a 3σ level.

469

470 Table 2

471 A brief summary of the difference between mica, pyrophyllite and chlorite.

	Spacing (Figs. 2,3)	HAADF (Fig. 4)	HRTEM (Fig. 5)	Mapping (Fig. 6)	Chemical composition
Chl	14 Å	14 Å Bright contrast	T: spots O/B: spots & lines	High Fe low K	$(R^{2+},R^{3+})_6(Si_{4-x}Al_x)_4O_{10}(OH)_8$ (Bailey, 1988)
Mica	10 Å	10 Å Dark contrast	T: spots O: spots & lines	High K Low Fe Low Mg	$(K, Na)_{x+y}(Mg,Fe^{2+})_x(Al, Fe^{3+})_{2-x}\square[Si_{4-y}(Al, Fe^{3+})_y]O_{10}(OH)_2$ (Rieder et al., 1998)
Py	9.5 Å	9.5 Å Dark	T: spots O: spots	High Al.Si Low Fe	$Al_2[Si_4O_{10}](OH)_2$ (Wardle and Brindley, 1972)

This is a preprint, the final version is subject to change, of the American Mineralogist (MSA)
Cite as Authors (Year) Title. American Mineralogist, in press.
DOI: https://doi.org/10.2138/am-2019-7074

	contrast	low K

Note: Chl: chlorite; Py: pyrophyllite; T: tetrahedral sheet; O: octahedral sheet; B: brucite-like sheet

Figure 1

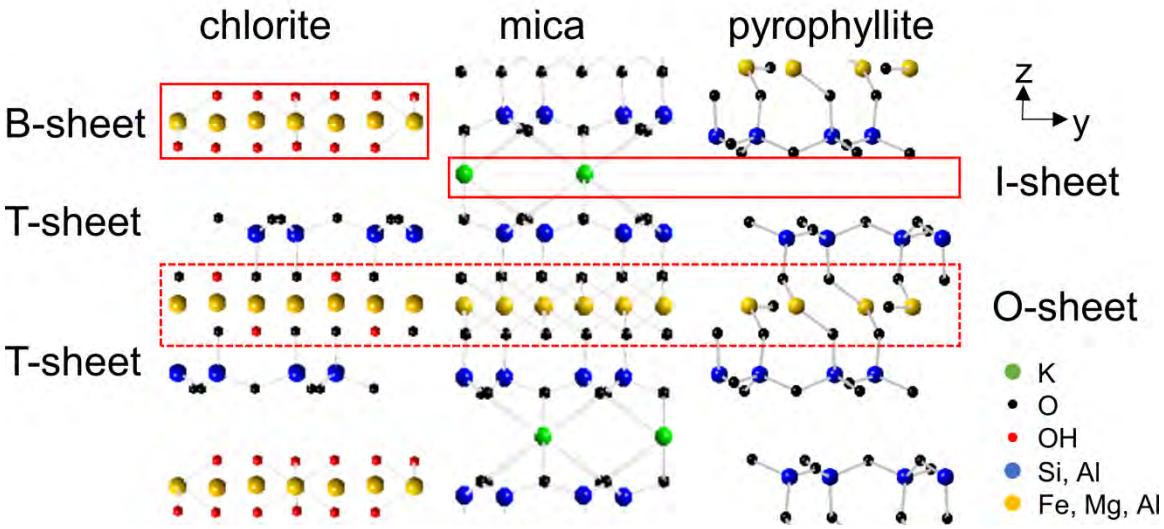

Figure 2

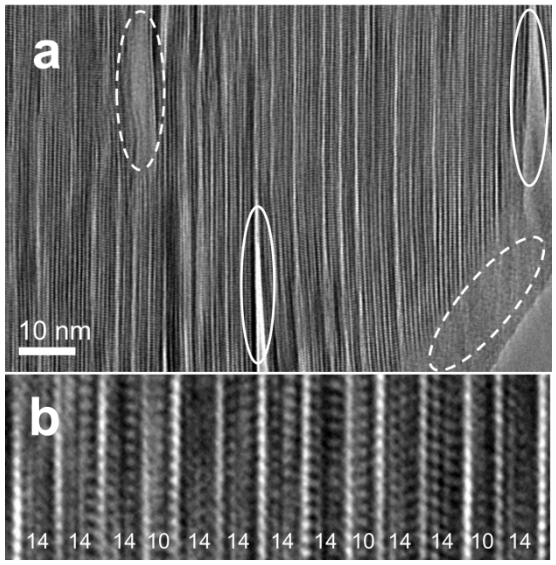

This is a preprint, the final version is subject to change, of the American Mineralogist (MSA)
Cite as Authors (Year) Title. American Mineralogist, in press.
DOI: https://doi.org/10.2138/am-2019-7074

Figure 3a

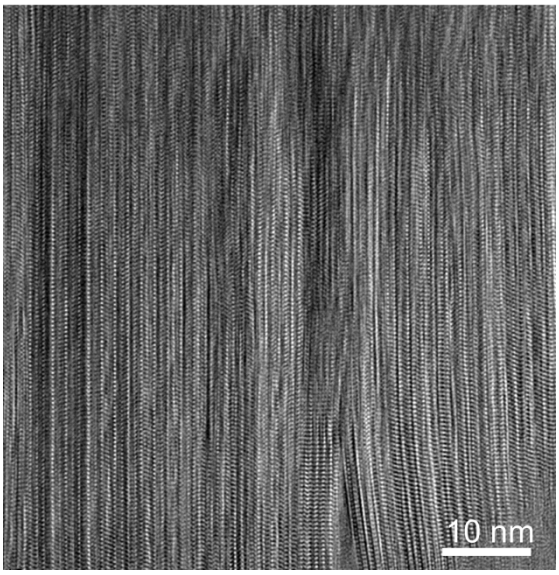

479

Figure 3b

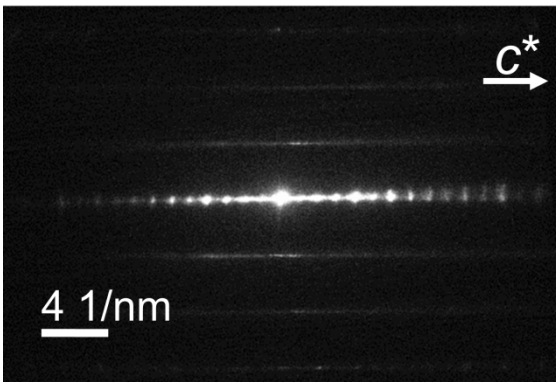

480

Figure 3c

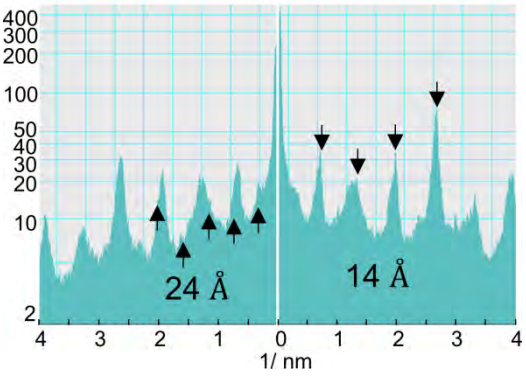

481

This is a preprint, the final version is subject to change, of the American Mineralogist (MSA)
Cite as Authors (Year) Title. American Mineralogist, in press.
DOI: https://doi.org/10.2138/am-2019-7074

Figure 4

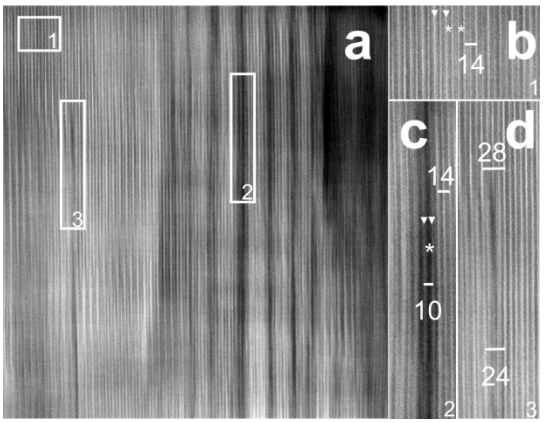

482

Figure 5

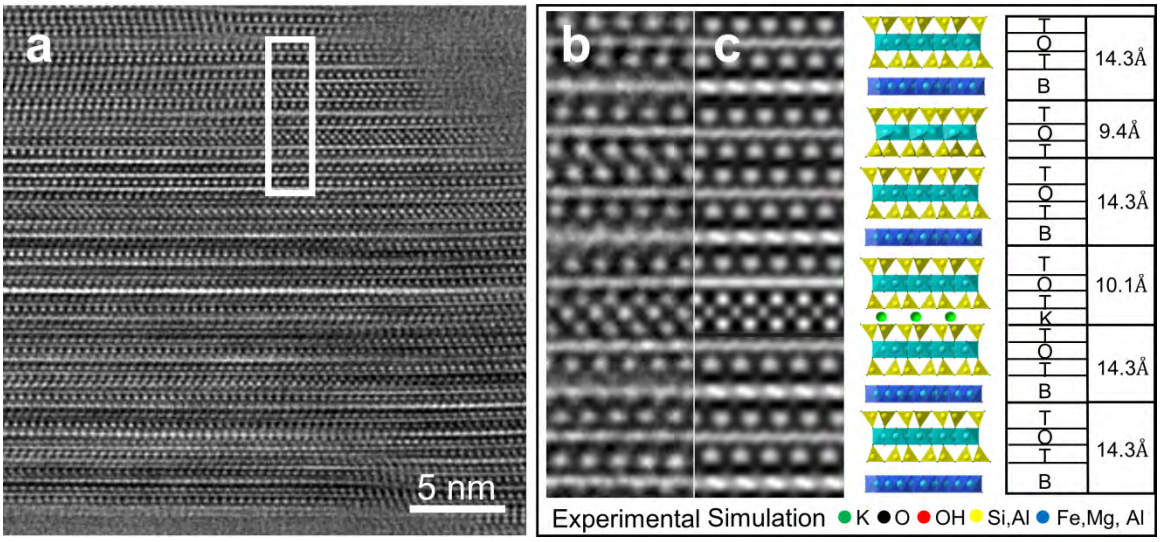

483

Figure 6a

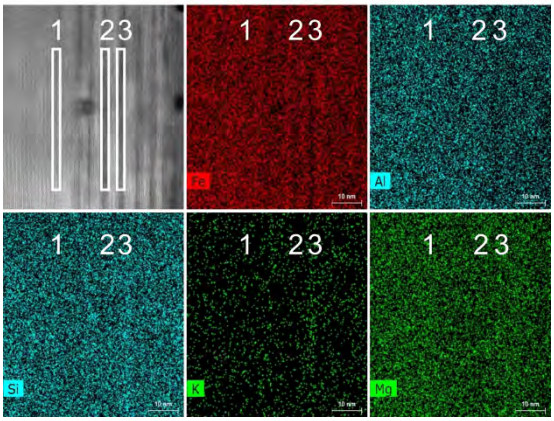

484

This is a preprint, the final version is subject to change, of the American Mineralogist (MSA)
Cite as Authors (Year) Title. American Mineralogist, in press.
DOI: https://doi.org/10.2138/am-2019-7074

Figure 6b

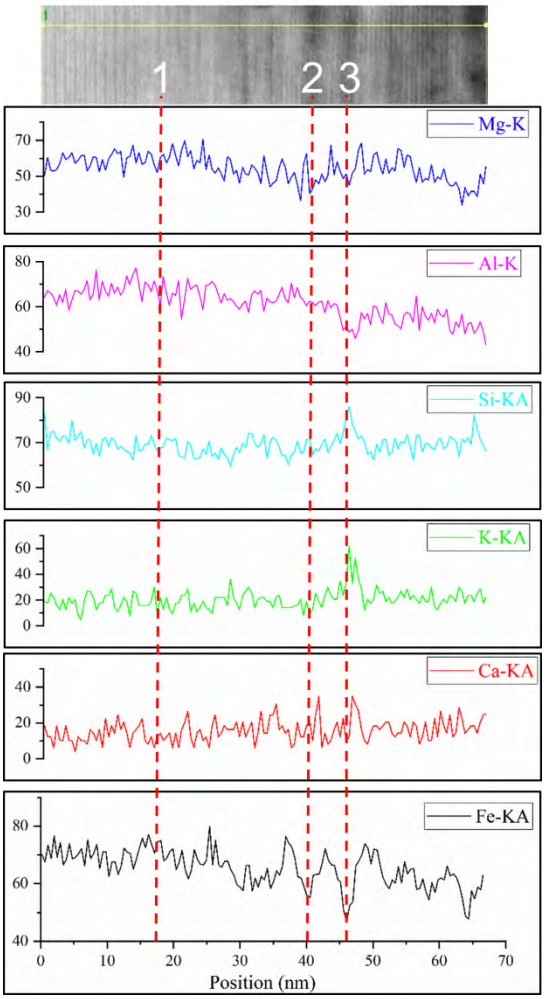

Figure 7

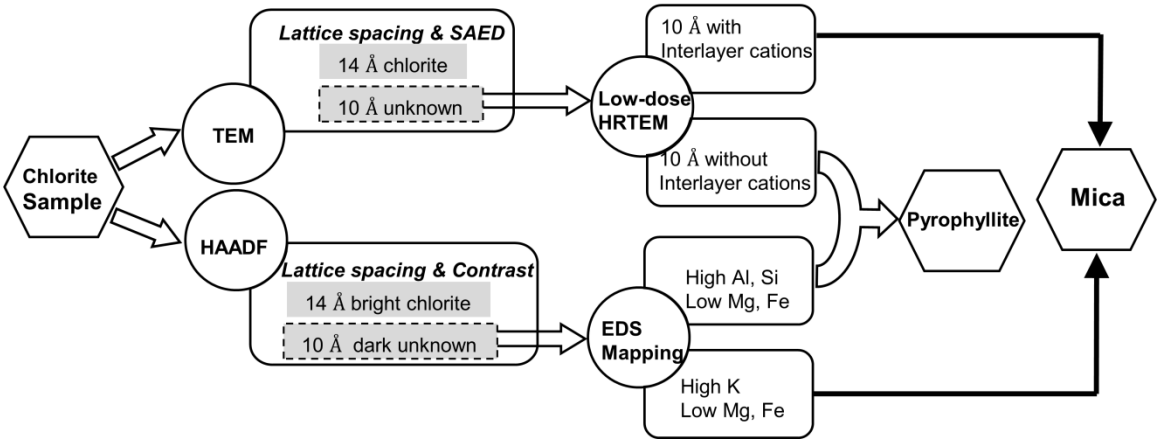

This is a preprint, the final version is subject to change, of the American Mineralogist (MSA)
Cite as Authors (Year) Title. American Mineralogist, in press.
DOI: https://doi.org/10.2138/am-2019-7074

Figure 8

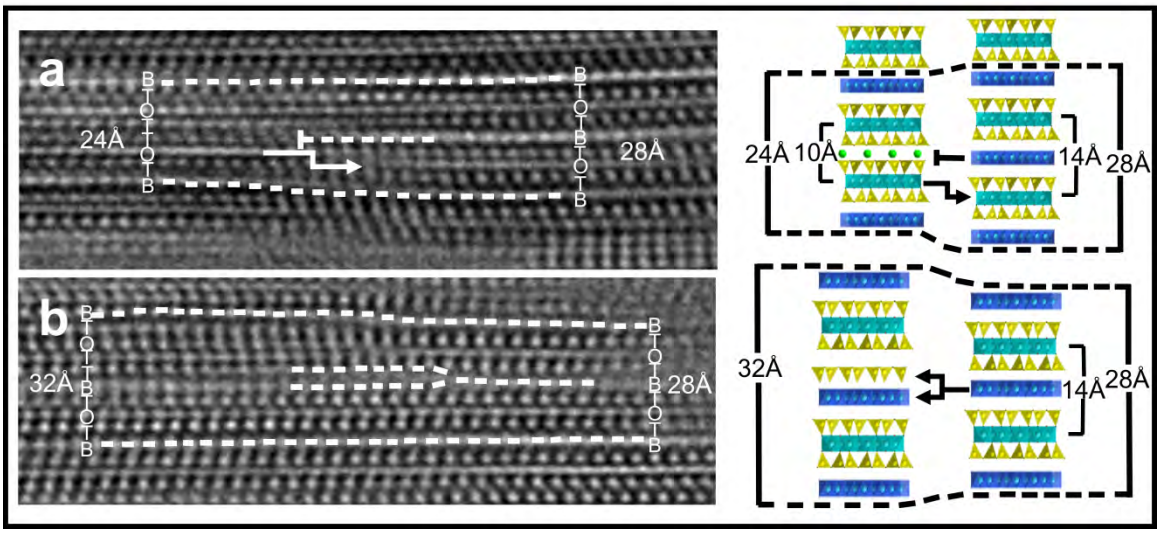

487

488